Analytical Methods

How to cite: *Angew. Chem. Int. Ed.* **2023**, *62*, e202310245
doi.org/10.1002/anie.202310245

Flexible, Miniaturized Sensing Probes Inspired by Biofuel Cells for Monitoring Synaptically Released Glutamate in the Mouse Brain

Prasad Nithianandam[+], *Tzu-Li Liu*[+], *Shulin Chen*[+], *Yizhen Jia, Yan Dong, Morgan Saul, Andrea Tedeschi, Wenjing Sun,* and Jinghua Li**

Abstract: Chemical biomarkers in the central nervous system can provide valuable quantitative measures to gain insight into the etiology and pathogenesis of neurological diseases. Glutamate, one of the most important excitatory neurotransmitters in the brain, has been found to be upregulated in various neurological disorders, such as traumatic brain injury, Alzheimer's disease, stroke, epilepsy, chronic pain, and migraines. However, quantitatively monitoring glutamate release in situ has been challenging. This work presents a novel class of flexible, miniaturized probes inspired by biofuel cells for monitoring synaptically released glutamate in the nervous system. The resulting sensors, with dimensions as low as 50 by 50 μm, can detect real-time changes in glutamate within the biologically relevant concentration range. Experiments exploiting the hippocampal circuit in mice models demonstrate the capability of the sensors in monitoring glutamate release via electrical stimulation using acute brain slices. These advances could aid in basic neuroscience studies and translational engineering, as the sensors provide a diagnostic tool for neurological disorders. Additionally, adapting the biofuel cell design to other neurotransmitters can potentially enable the detailed study of the effect of neurotransmitter dysregulation on neuronal cell signaling pathways and revolutionize neuroscience.

Introduction

Biofluids contain a diverse range of chemical biomarkers that can provide insights into health and age-related conditions. These biomarkers are highly relevant to fields such as biomedical research, advanced healthcare, and clinical medicine.[1] Continuous monitoring of biomarker levels, in particular, can offer valuable evidence that enables the effective diagnosis and treatment of chronic diseases and injuries. As one example, glutamate is one of the most important excitatory neurotransmitters in the mammalian central nervous system (CNS) that is responsible for learning, memory, and communication between neurons.[2] However, excessive glutamate can lead to hyperexcitability of post-synaptic neurons, resulting in induced excitotoxicity.[3] This phenomenon can result in decreased neuronal regeneration and dendritic branching which can not only impair memory and cognition but increase the risk of the development of various neurological diseases. Accordingly, elevated glutamate concentrations show a strong correlation with many neurological disorders, such as traumatic brain injury (TBI), Alzheimer's disease, stroke, epilepsy, chronic pain, and migraines.[4] In patients who have suffered an ischemic stroke and neurological deterioration, glutamate concentrations in the brain can increase from 15 to 200 μM, and in plasma from 100 to 300 μM. Glutamate concentrations that exceed 200 μM in plasma can serve as a predictor of neuronal damage progression at 48 h post-stroke.[5] Thus, the development of an implantable glutamate sensor that can relay real-time glutamate concentration levels to medical professionals would aid in both the diagnosis and prevention of stroke in high-risk patients (e.g., smokers, patients with high cholesterol or blood pressure).

However, the accurate, continuous, and real-time measurement of glutamate in situ remains a challenging topic. Conventional techniques, such as glutamate microdialysis and ultraperformance liquid chromatography-tandem mass spectrometry (UPLC-MS/MS), have limited capability for

---

[*] P. Nithianandam,[+] T.-L. Liu,[+] S. Chen,[+] Y. Jia, Dr. Y. Dong
Department of Materials Science and Engineering,
The Ohio State University
Columbus, OH 43210 (USA)

M. Saul, Dr. W. Sun
Department of Neuroscience, Wexner Medical Center, The Ohio State University
Columbus, OH 43210 (USA)
E-mail: wenjing.sun@osumc.edu

Dr. A. Tedeschi
Department of Neuroscience, Wexner Medical Center, Chronic Brain Injury Program, The Ohio State University
Columbus, OH 43210 (USA)

Dr. J. Li
Department of Materials Science and Engineering,
Chronic Brain Injury Program, The Ohio State University
Columbus, OH 43210 (USA)
E-mail: li.11017@osu.edu

[+] These authors contributed equally to this work.

real-time monitoring of subtle changes in glutamate concentration with a spatial resolution. Recently developed glutamate sensor protein, iGluSnFr, enables the optical measurement of glutamate dynamics. However, it only measures glutamate semi-quantitatively without providing an absolute concentration reading and needs genetic modification of the subject.[6] Through the use of electrochemical amperometry techniques, alternative strategies have successfully leveraged biosensors to continuously monitor glutamate release in real-time and/or explore their correlations with electrophysiological signals.[7] Despite the great advances enabled by pioneering studies, the existing approaches still involve a complex collection of on-chip hardware for signal generation, such as potentiostats, and power supply/management systems. The difficulty in minimizing the form factors of these subsystems poses substantial challenges in achieving the goal of building miniaturized and lightweight neural interfaces for understanding and intervening in various neurological diseases.

To address this issue, this work presents a class of flexible, miniaturized probes inspired by the structure and working principle of biofuel cells for monitoring synaptically released glutamate in the nervous system.[8] The sensor exploits an enzyme functionalized sensing interface, where the anodic and cathodic reactions will spontaneously generate electrical currents proportional to the concentration of glutamate in the solution. The elimination of potentiostat simplifies the measurement setup compared to that for conventional three-electrode electrochemical cells. Systematic studies investigate the structure-performance interrelationship of the enzyme-functionalized interface for quantitative analysis. The resulting sensors, with dimensions as small as 50 by 50 μm, can detect real-time changes in glutamate within the biologically relevant concentration range (μM level in cerebrospinal fluids (CSF),[4c] μM–mM level near synaptic vesicle release sites).[7a,d] Ex vivo experiments using the hippocampal circuit in mice models demonstrate the capability of the sensors in monitoring glutamate release during synaptic transmission in electrically stimulated acute brain slices. By functioning as sensing media for brain-machine interfaces, the resulting devices have the potential to improve our understanding of the underlying molecular and cellular mechanisms of structural and functional maladaptive changes in neural circuits after a variety of CNS trauma and diseases. This knowledge can shed light on the development of new therapeutic interventions for these pathological conditions.

Results and Discussion

Working principle and fabrication procedures of the glutamate biofuel cell sensors

The previously reported biofuel cell structure in the literature inspires the design of the glutamate sensors developed in this work, where glutamate spontaneously generates electrical signals proportional to the concentration.[9] Figure 1 illustrates the primary components and the working principle of the sensing platform. The anode is composed of a gold layer, a rough electrically conductive layer to increase the surface area (either platinum black (Pt-black) or carbon nanotubes (CNTs)), a redox mediator layer containing tetrathiafulvalene (TTF) for electron transfer, an enzyme layer containing immobilized glutamate oxidase (GlutOx) linked to bovine serum albumin (BSA), and a protective layer of Nafion against interferent molecules. Specifically, a rough, electrically conductive surface is essential for the transfer of electrons from the redox mediators and enzyme layers to the gold electrode, as well as to increase the surface area for the attachment of enzymes. The redox mediator TTF aids in the transfer of electrons from glutamate that has reacted with GlutOx to the electrode. The enzyme layer contains GlutOx as the catalyst and BSA conjugated to GlutOx to minimize leaching to the surrounding solution. The reaction mechanism for the oxidation of glutamate is as follows:

$$\begin{aligned}&\text{L-glutamate} + \text{GlutOx}_{\text{ox}} + \text{O}_2 + \text{H}_2\text{O} \rightarrow \\ &\text{2-oxoglutarate} + \text{NH}_3 + \text{H}_2\text{O}_2 + \text{GlutOx}_{\text{red}}\end{aligned} \tag{1}$$

$$\text{TTF} \rightleftharpoons \text{TTF}^+ + \text{e}^- \tag{2}$$

$$\text{GlutOx}_{\text{red}} + \text{TTF}^+ \rightarrow \text{GlutOx}_{\text{ox}} + \text{TTF} \tag{3}$$

Glutamate undergoes oxidation to produce 2-oxoglutarate (2-OG), ammonia and hydrogen peroxide which simultaneously converts GlutOx into a reduced form.[10] TTF goes through a reversible reaction in which it exists in chemical equilibrium between TTF and TTF^+ once immersed in the solution. TTF^+ reacts with the reduced form of GlutOx, and the reaction converts the enzyme and TTF back to their original states.

The cathode is composed of a gold layer, a rough electrically conductive surface layer of either Pt-black or CNTs, a platinized carbon (Pt-C) layer, and a layer of Nafion. The functions of the Nafion and Pt-black/CNT are similar to those in the anode, and the Pt-C layer acts as a catalyst for the reduction of oxygen to water. The anodic and cathodic reactions generate electrical currents proportional to the concentration of the glutamate. A load resistor connecting the anode and cathode transforms the current into a voltage for signal readout using an electrochemical workstation.

Figure 2A illustrates the procedures for the preparation and functionalization of the electrodes with detailed information provided in the Experimental Section. After the preparation of the conductive layer on the gold electrode, drop-casting TTF yields a thin redox mediator layer on the surface. Then, drop-casting a mixture of BSA, Nafion and GlutOx followed by drying the system at 4 °C for a day forms the enzyme coating layer. To prepare the cathode, drop-casting a solution of Pt-C and Nafion deposits the catalyst for the reduction of oxygen. Figure 2B–G display scanning electron microscope (SEM) images illustrating the immobilization of key functional layers on the rough conductive electrode surfaces. The Supporting Information contains detailed information about the procedures for

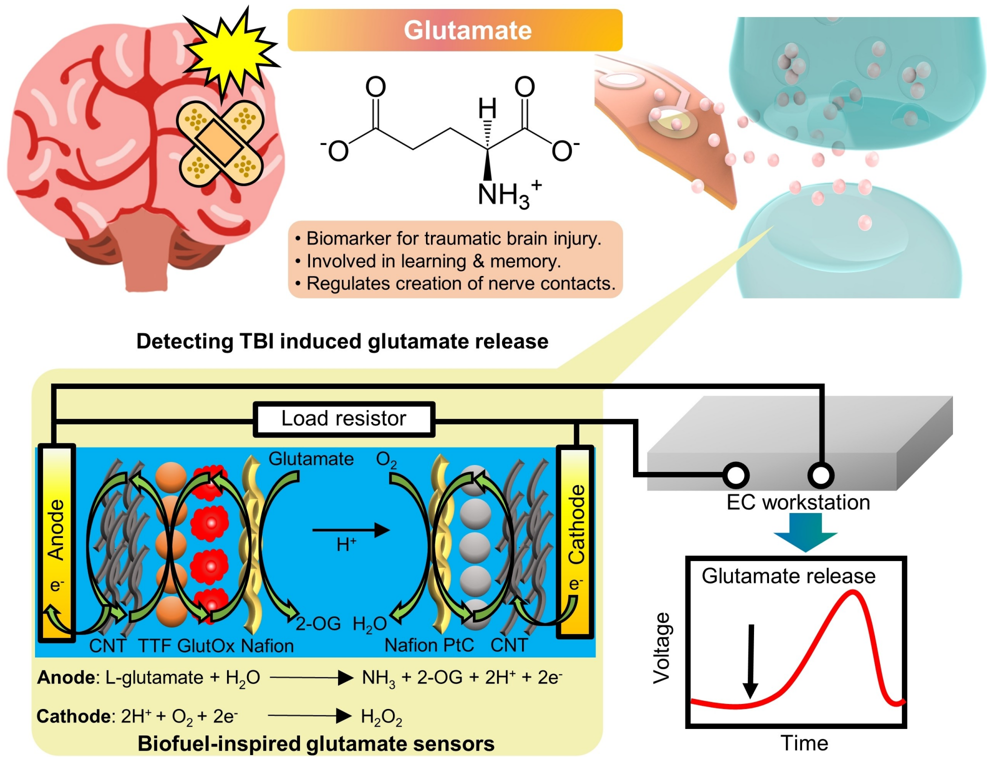

Figure 1. Conceptual illustration of monitoring glutamate release during synaptic transmission in extracellular space using the flexible, miniaturized glutamate sensors and the working principle of the sensing platform inspired by the design and structure of biofuel cells.

functionalization. The functional materials play an important role in facilitating the redox reactions at the cathode and anode and as the fundamental components of the biofuel cell structure for glutamate sensing.

Sensing performance characterization of the glutamate sensors

The glutamate biofuel cell sensors operate by measuring the voltage across the load resistor that connects the anode and cathode. This voltage corresponds to the glutamate concentration, with higher concentrations yielding higher signal readouts. First, we assess the performance of the sensors in solutions with the known concentration of glutamate (Figure 3). Testing of the sensor with a pair of commercial Au disk electrodes (diameter: 2.5 mm) takes place by periodically adding 50 μM glutamate every 200 s in 1X phosphate-buffered saline (PBS) while recording the stepwise change in potential (Figure 3A–C) (load resistor: 100 kΩ). The sensor has a working range of 0.05 mM to 1.2 mM, with a linear response in the range of 0.6 mM to 1.0 mM. Figure 3B serves as a detailed representation of the voltage response within the low glutamate concentration range depicted in Figure 3A. It demonstrates that the sensor can provide a measurable response even when exposed to low concentrations of glutamate. Extracting the slope of the curve within the linear range of detection yields a sensitivity of 5.1721 $\mathrm{mV\,mM^{-1}}$. Calculating the standard deviation of the baseline of equilibrated signals estimates the noise level (0.012 mV). The limit of detection (LOD), which is the lowest concentration of an analyte in a sample that can be detected with a stated probability,[7a] is 0.0069 mM, as estimated using the equation 3 X (the noise of the system/ the sensitivity of the system).

The trend observed is that, at lower glutamate concentrations (0.05 mM to 0.6 mM), there is a slight increase in potential because the current generated from the enzymatic reaction is minimal, as glutamate only binds to a small number of active sites of GlutOx. Similarly, at higher concentrations (1.0 mM to 1.2 mM), the response in potential is lower due to the surface saturation. Such biofuel cell sensors have the potential to encompass physiologically relevant concentration ranges of glutamate in the CNS system as previous studies have reported the concentration of glutamate in the synaptic cleft to be 1 mM, while the ambient concentration in CSF ranges from ≈2.54 to 6.51 μM.[11]

Increasing glutamate concentration in a stepwise fashion (250 μM) and then reducing it to 0 afterward for three consecutive cycles investigates the reversibility of the glutamate sensors (Figure 3D). The results indicate that the sensing platform has a sensitivity of approximately 2.77 $\mathrm{mV\,mM^{-1}}$ throughout the three cycles and returns to a similar baseline after being placed back into fresh PBS solution. Figure 3E shows cyclic voltammetry scans of the anode with increasing glutamate concentration added in 1X PBS, with a sensitivity of 77.17 $\mathrm{\mu A\,mM^{-1}\,mm^{-2}}$ (Figure S1). The amplitude of the oxidation peak at 0.35 V becomes

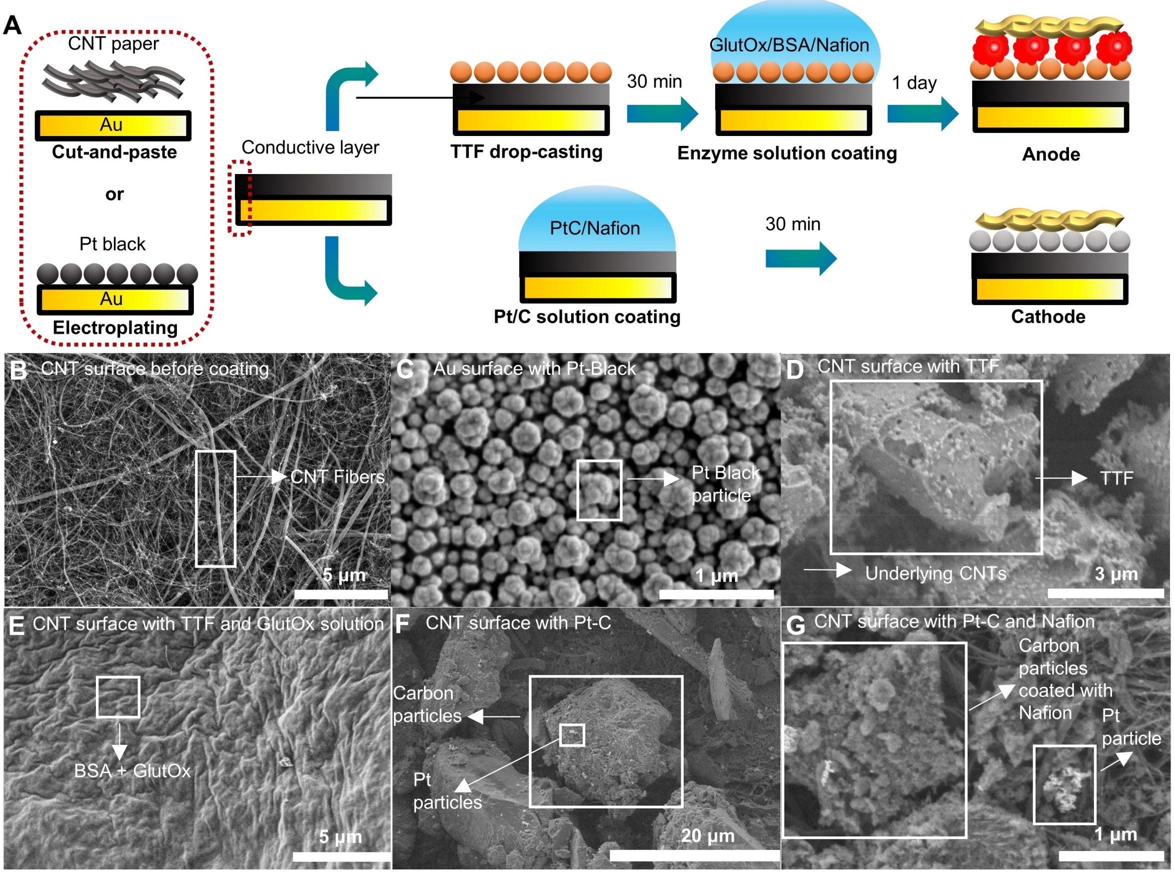

Figure 2. Structure of the functional interface materials in the anode and cathode, and the changes in the surface morphology during the fabrication process. (A) Schematic illustration showing the functionalization protocol of active components onto the surface of the anode and cathode. (B) SEM image of CNT surface showing the fibrous structure before functionalization. (C) SEM image of the structure of an Au electrode surface after the electrodeposition of Pt-black as an alternative conductive layer. (D) SEM image of an anode showing large TTF agglomerates interspersed within the CNT network. (E) SEM image of an anode after the addition of the enzyme layer that covers both the underlying CNT network and the TTF agglomerates, leading to a smooth surface morphology. (F) SEM image of a cathode showing Pt-C drop-cast onto the CNTs, with small Pt particles on the surface of the large carbon particles. (G) SEM image of a cathode presenting the surface of CNT with both Pt-C and Nafion deposited, with the surface of the Pt-C particles appearing rougher due to the addition of Nafion.

larger as the glutamate concentration increases from 0.2 to 0.5 mM. This oxidation peak corresponds to that of TTF, consistent with previous reports in the literature, further confirming the function of TTF in electron shuttling.[12] Specifically, this work utilizes the biofuel cell structure for the sensing mechanism of glutamate instead of using amperometry. This choice is motivated by factors such as compatibility for miniaturization and battery-free operation due to the working principle of biofuel cells. These characteristics bring simplification to the required electronics compared to conventional amperometric sensors. Consequently, this approach holds promise for integration into wireless sensing platforms based on near-field communication (NFC) technology.[9a] Such advantages are particularly relevant in neuroscience applications that prioritize compact, lightweight biosensors. While this work highlights the advantages of the biofuel cell sensors for glutamate sensing, it is important to note that these advantages do not automatically imply that voltage response is better than amperometry. The choice of sensors should be based on the specific context and requirements of the application at hand. Factors such as dimensions, sensitivity, selectivity, response time, dynamic range, and LOD must be carefully considered to determine the most suitable sensor for a given situation.

Storing freshly prepared sensors in 1X PBS at 4 °C helps retain the bioactivity of enzymes. Figure 3F and 3G show the lifetime of such sensors in a liquid environment. The results suggest that the sensor can maintain 90 %, 80 %, and 70 % of its original sensitivity on day 0 for 4, 8, and 14 days, respectively. Eventually, the system loses 95 % of its sensitivity on day 46, possibly due to the leaching of functional components into the solution. The additional data in Figure S2 provides further insights into the stability of the sensor over time. The values of relative stability, 90 % and 93 % on day 2 and 4, respectively, highlight the stability of the sensor for at least 4 days.

Figure 3H showcases the performance of the sensor in artificial CSF (aCSF) at body temperature (37 °C). Increasing the amount of glutamate to 4.73 µM (which is at the same order of magnitude as the concentration found in

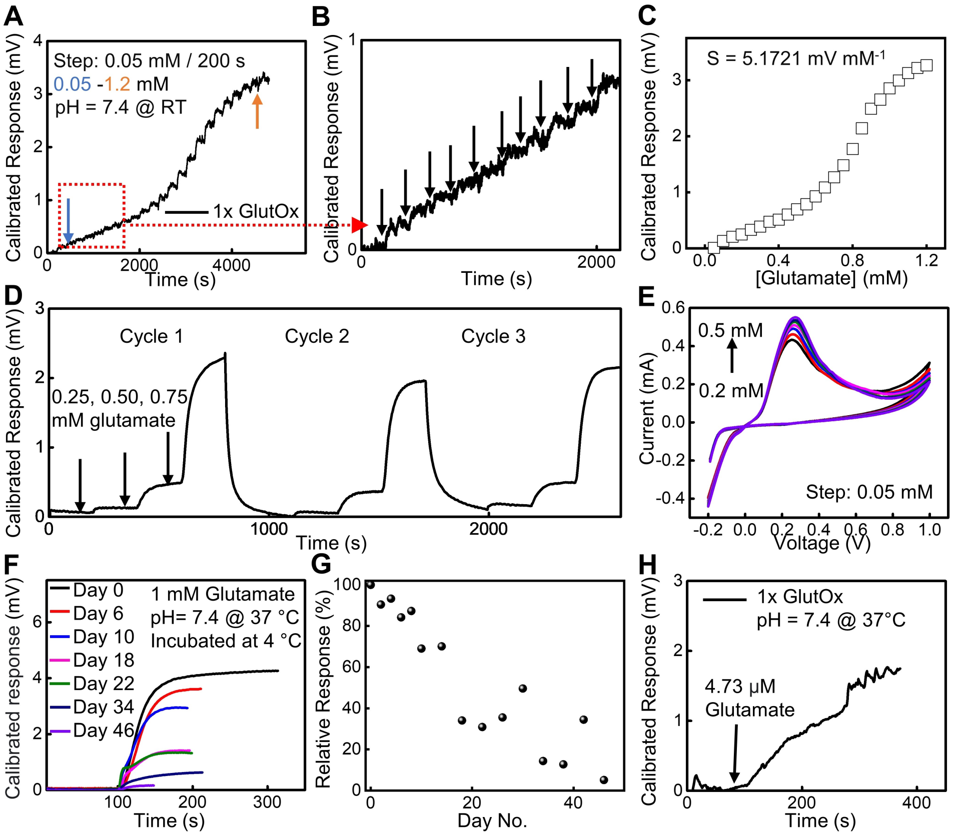

Figure 3. Performance characterization of the glutamate biofuel cells. (A) Change in potential (calibrated response) as a function of time when the glutamate concentration increases by 0.05 mM every 200 s. (B) Magnified view of (A) from 0 to 2000 s, where the arrows indicate the point of glutamate addition. (C) Calibration curve of glutamate biofuel cell with a sensitivity of 5.1721 mV mM^{-1}. The load resistance is 100 KΩ.
(D) Reversibility test whereby 0.25 mM of Glutamate is added into the glutamate biofuel cell. After 3 additions, the biofuel cell is placed in fresh 1X PBS. The data during the three sensing cycles are collected separately with a pause between each cycle and plotted together for comparison.
(E) Cyclic voltammetry performed from 0.2 mM to 0.5 mM glutamate in 0.05 mM steps from −0.2 V to 1.0 V with a scanning rate of 0.1 V s^{-1}.
(F) Stability test showing a response of a glutamate biofuel cell to 1 mM of Glutamate for a period of 46 days. (G) Decay in relative response (%) as time progresses. (H) Response of the glutamate biofuel cell to a glutamate concentration similar to that found in CSF (4.73 μM). The load resistance is 10 MΩ.

ambient CSF according to the literature)[11a] induces an increase in potential. Two reasons account for the larger response observed in Figure 3H compared to Figure 3A. (1) The device in Figure 3H is equipped with a 10 MΩ load resistor, while Figure 3A utilizes a 100 KΩ resistor. This allows the response to exceed the lower detection limit of the EC station. (2) The temperature used in the experiment in Figure 3H is 37 °C, as opposed to 25 °C in Figure 3A. The higher temperature enhances enzymatic activity, resulting in a lower value of LOD than what is calculated based on the data in Figure 3A. Overall, the performance characterization presented here suggests the feasibility of using the biofuel cell sensor for detecting glutamate at physiologically relevant concentrations.

Structure-performance interrelationship of biofuel cell sensors

Systematic studies investigate key parameters impacting the performance of the biofuel cell sensors with a summary presented in Figure 4A. Figure 4B and S3 demonstrate the impact of TTF concentration on sensitivity, with results indicating that increasing the TTF concentration leads to a decrease in sensitivity (a decrease of 5.1721 mV mM^{-1} at 20 mg mL^{-1} to 0.6676 mV mM^{-1} at 30 mg mL^{-1}). One possible explanation is that a lower concentration of TTF may lead to the crystallization of TTF particles at a smaller size, maximizing the surface area available for catalyzing the reaction.[13] Figure 4C and S4 illustrate the difference in sensitivity between body temperature (25.327 mV mM^{-1} at 37 °C) and room temperature (5.1721 mV mM^{-1} at 25 °C) in 1X PBS. The extracted value is ≈5 times higher at the higher temperature due to both the increased diffusion rate of the substrate[14] and the elevated activity of the enzyme.[15] Figure 4D and S5 show the effect of adding 5 times the amount of enzyme solution to the surface of the electrode. While the sensitivity is only slightly higher (5.17 mV mM^{-1} for the original vs. 5.74 mV mM^{-1} for the 5X amount), the more significant benefit is the reduced noise level (0.012 mV for the original vs. 0.00476 mV for the 5X amount), which is attributed to both the enhanced charge transfer and an additional amount of Nafion mixed with the enzyme

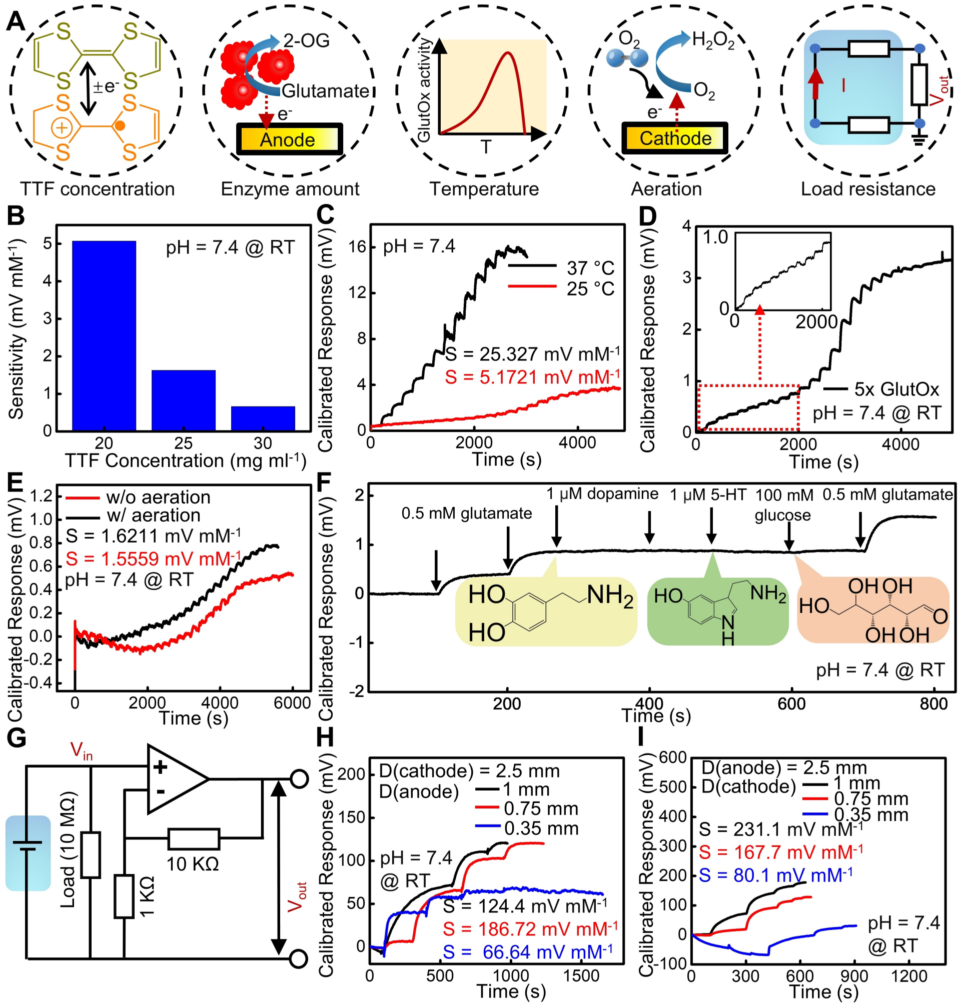

Figure 4. Impact of key parameters for optimization of the biofuel cell performance. (A) Schematic illustration showing key parameters explored in this study impacting the performance of the biofuel cell glutamate sensors. (B) Effect of different TTF concentrations on the sensitivity of the glutamate biofuel cell. (C) Effect of temperature on sensitivity of the glutamate biofuel cell: body temperature (37 °C) and room temperature (25 °C). The red curve is the same as in Figure 3A for comparison. (D) Change in potential vs. time for a glutamate biofuel cell with 5× enzyme amount of that used in Figure 3A. (E) Effect of aerating the solution for 5 minutes before characterization on the biofuel cell performance showing the importance of O_2 for eliminating the initial signal drift. (F) Performance of a biofuel cell in the presence of interferents such as dopamine, serotonin (5-HT) and glucose at physiologically relevant concentrations. (G) Schematic illustration of the differential amplifier utilized to amplify signals for miniaturized electrodes. (H) Effect of reducing anode diameter to 1 mm, 0.75 mm and 0.35 mm while the cathode diameter is kept constant at 2.5 mm. (I) Effect of reducing cathode diameter to 1 mm, 0.75 mm and 0.35 mm while the anode diameter is kept constant at 2.5 mm.

solution as the surface passivation layer. One possible theoretical basis is that increasing the enzyme concentration can lead to a larger number of available active enzyme sites for catalysis and electron transfer. This, in turn, enhances the overall rate of the enzymatic reaction and improves electron transport efficiency. Additionally, a previous study suggests that the limiting steady-state current of enzyme-functionalized electrodes is correlated with the surface concentration of the enzyme (C_E) according to the following equation:

$$i_{enz} = \pm n_S F A \frac{k_c C_E}{1 + \frac{K_s}{c_S}} \tag{4}$$

Where n_S is the number of electrons, F is the Faraday constant, A is the electrode surface area, k_c is the catalytic constant, K_s is the Michaelis constant, c_S is the concentration of substrate.[16] These results contribute insights to the field of enzyme-functionalized electrode design and pave the way for realizing analytical tools with improved performance.

The effect of aeration of the test solution on sensor performance appears in Figure 4E and S6. The sensor response shows drift without aeration, while no such decrease in potential presents for sensors with aeration. The initial decrease in potential may be due to voltage reversal, which can occur when there is insufficient substrate (i.e., glutamate) or insufficient oxygen (i.e., the "oxygen starvation" effect) for the cathodic reaction to occur, resulting in the undesired switch in the polarity of the sensors.[17] To describe the mechanism of glutamate quantification in detail, Figure S6A–D present the analysis of the linear response range of the devices in Figure 4E. Additionally, while it is common to design sensors with a linear working range within the physiologically relevant concentration of biomarkers for practical applications,[9a] a comprehensive understanding of the sensing performance across the entire concentration range provides insights into its performance characteristics and limitations. The fittings of the entire response curves using the Lorentz function and Sigmoid logistic function appear in Figure S6E–F, respectively. The quantitative equations reveal the interrelationship between glutamate concentration and the output voltage and the effect of oxygen pressure.

Figure 4F illustrates the capability of Nafion in protecting the fuel cell from interfering molecules such as dopamine, serotonin and glucose with physiologically relevant concentrations to ensure a high selectivity.[18] Previous studies have reported the physiological concentrations of dopamine and serotonin for dopaminergic and serotonergic neurons during an action potential are 0.25 μM and 0.1 μM, respectively,[19] which justifies the selection of concentrations of interferents used here. The variation in voltage response to glutamate can be attributed to the non-linear sensing performance observed across the concentration range investigated in this study. Figure S7 presents more results of supplementary experiments conducted with ascorbic acid (10 μM) and DOPAC (10 μM) as interferents, utilizing concentrations reported in previous literature.[20] These results further demonstrate the high selectivity of the sensors, as the responses to these interferents are minimal in comparison to the observed changes in potential in response to glutamate. The mechanism of Nafion in keeping the fuel cell from interferents may be as follows: (1) Nafion has excellent barrier properties against small molecules and proteins.[21] By incorporating Nafion as a protective layer on top of TTF, it can help prevent the diffusion or adsorption of interferents (especially electroactive species such as dopamine and serotonin) onto the sensing electrode.[9a] (2) Nafion possesses strong ion exchange capabilities, which allow it to selectively transport specific ions while blocking others.[22] This property can enhance the selectivity of the biofuel cell sensor by selectively allowing the passage of glutamate while minimizing interference from other substances. In addition to Nafion, other surface passivation materials, such as BSA, may also be important blocking nonspecific interactions and improving the selectivity of the system. Optimization of these parameters can lead to enhanced selectivity in biofuel cell sensors.

To ensure minimal invasiveness of the neural interface to surrounding bio-tissues in animal models, the design of miniaturized electrode pairs is highly desirable. Pt-black provides a realistic option for creating the biochemical interface on miniaturized electrodes through electrodeposition. Figure S8 shows the performance of utilizing electrodeposited Pt-black nanoparticles on a commercial gold electrode as a replacement for CNTs on the biochemical interface with the functionalization protocol kept constant. Initially, a voltage decrease occurs due to voltage reversal upon increasing the glutamate concentration. However, from a concentration of 0.4 mM onwards, any increase in glutamate concentration causes a rise in potential as expected.

Figure 4G–I provide insight into the effect of scaling the electrode dimension on the sensing performance. Specifically, these Figures highlight the sensitivity difference by systematically varying the anode and cathode size, respectively, while keeping the size of the other electrode constant at 2.5 mm in diameter. Controlling the amount of enzyme solution/Pt-C and Nafion mixtures added to the electrodes ensures the same density of surface functional components in all groups. Decreasing the surface area of the electrode results in an increase in electrode resistance. For example, when the surface area decreases from 0.442 mm^2 to 0.096 mm^2, the impedance increases from approximately 4.6×10^4 to 3×10^6 Ω, as shown in Figure S9 (please note that the surface area of the opening for the 1000-micron electrode is 0.244 mm^2, and that of the 750-micron electrode is 0.442 mm^2 due to a small amount of UV gel flowing into the 1000 micron aperture, thereby decreasing the biochemical interface area). To avoid the voltage division effect across the solution-sensor interface caused by large increases in impedance, replacing the 100 kΩ resistor with a 10 MΩ alternative can be helpful in more efficiently collecting voltage signals for miniaturized electrodes. Additionally, implementing a differential amplifier with a 10× gain across the load resistor further amplifies the signal and maximizes the signal-to-noise ratio (Figure 4G and S10). The progressive increase in impedance with decreasing effective surface area for both the anode and cathode explains the phenomenon of decreasing sensitivity (Figure 4H–I) due to restricted current flow. Specifically, the sensitivity decreases from 186.72 to 66.64 mV mM^{-1} the anode diameter decreases from 1 to 0.35 mm, and the value decreases from 231.11 to 80.1 mV mM^{-1} when the cathode diameter decreases from 1 mm to 0.35 mm.

Notably, decreasing the anode diameter to 0.35 mm shifts the dynamic range of the sensor towards lower concentrations (Figure 4H). One possible explanation for this phenomenon is that a smaller anode dimension makes it easier to saturate the active sites on the anode surface. As a result, even a small increase in glutamate concentration can lead to a relatively large initial response from the sensor. This occurs as the sensor quickly enters the linear response range, exhibiting a more sensitive and responsive behavior at lower concentrations. For the device with a cathode diameter of 0.35 mm (Figure 4I), the initial downward trend could be attributed to the O_2 starvation effect resulting from the reduction in cathode size.[9b] As the cathode size decreases, the availability of O_2 for the reduction reaction may become limited, causing a decrease in the sensor response at lower glutamate concentrations. This decrease in response can manifest as an initial drift in the readings until the O_2 supply reaches equilibrium.

Figure S11 further highlights the importance of aeration for optimal cathodic performance. Since protons and oxygen are reduced to water at the cathode, insufficient aeration can result in a limited sensor response, particularly at lower glutamate concentrations. This is demonstrated by the differences in sensing performance without and with aeration, where the former is not able to quantify glutamate at concentrations between 0.2 and 0.4 mM.

Figure S12 showcases the performance of a thin film electrode when both the diameter of the anode and cathode are miniaturized to 500 μm. The miniaturized device displays a sensitivity of 185.98 $\mathrm{mV\,mM^{-1}}$ and can detect glutamate at low concentrations of 0.015 mM.

Testing of performance of microfabricated probes in mouse brain homogenate

The knowledge and understanding acquired in the preceding sections have informed the design and development of sensing probes on polymeric substrates using standard microfabrication techniques in a high throughput manner (Figure 5A). Briefly, the fabrication of the glutamate probes involves laminating a flexible Kapton film on a glass slide with uncured polydimethylsiloxane (PDMS) and heating it to form the substrate. Subsequent deposition, lithographic patterning, and etching yield thin-film Cr/Au electrodes as the cathode and anode. Functionalizing the electrodes based on the protocols described earlier completes the fabrication process of the glutamate probes. Further details about the fabrication process are in the Experimental Section.

Characterizing the performance of the biofuel cell probes in brain tissue ex vivo assesses their capability of operating in a complex biological environment. Homogenizing a mouse brain in 1 mL aCSF followed by centrifuging the sample (10,000 RPM for 10 minutes) yields supernatants providing a tissue environment. The use of a commercial assay kit (MAK004, Sigma Aldrich) to test brain homogenates (diluted 5-fold) indicates a glutamate concentration of 1.018 mM (Figure S13A). As the concentration of glutamate in the brain homogenate falls outside the detection limit of the biofuel cell, a 50X dilution of the homogenate to a concentration of 0.1 mM is necessary to establish the baseline calibration. Adding concentrated glutamate (1 M) into the base solution forms a series of test solutions for the characterization of the probes. Comparing the accuracy for determining the glutamate concentration in the diluted brain homogenate with the commercial glutamate assay evaluates the performance of the microfabricated probes (Figure 5B). Figure 5C showcases the brain homogenate sample following centrifugation while the image on the bottom right corner is a microscope image of the probe (electrode diameter: 500 μm). Figure 5D and 5E show the calibration plots for a pair of 500 μm diameter electrodes obtained in 1X aCSF and brain homogenate (50X dilution), respectively. The extracted sensitivity is 272 and 109 $\mathrm{mV\,mM^{-1}}$, as summarized in Figure 5F. The discrepancy might be due to the presence of interferents in the complex biological environment. Figure 5G shows the Pearson's coefficient ($r = 0.960246$) between the added glutamate concentration and the calculated glutamate concentration based on the calibration curve of the probe in aCSF. Figure S13B–C present results obtained using a similar experimental design but with the commercial assay kit. Figure 5H presents the comparison between the glutamate concentration measured using the probe and the glutamate assay kit in a 50X brain homogenate dilution, yielding a p-value of 0.136. The slight discrepancy observed may be attributed to the surface saturation issue of the sensor at the biochemical interface, whereas the commercial assay allows for uniform spreading of analytes in the wells. Nevertheless, the results of the validation experiments in brain homogenate suggest that the probes inspired by biofuel cells have the potential to quantitatively measure glutamate in brain tissues during future in vivo studies.

Ex vivo studies of glutamate release from the hippocampal circuit in mice

Building on the successful development of glutamate sensors, the study leverages these probes to quantitatively analyze the release of glutamate from acute mouse brain slices. Further scaling down the form factors of the probes to nearly cellular-scale dimensions (as small as 50 by 50 μm for the sensing area) enhances the spatial resolution and biocompatibility for future in vivo applications. This will enable real-time visualization of changes in glutamate concentration at the tissue-device interface. Figure 6A and 6B show a microscopic image and a photograph of a representative probe in a bent configuration, while additional photographs appear in Figure S14, respectively, providing a visual representation of the size and design parameters of the probes. Figure 6C shows a mechanical test of the probe using a brain model made of a 0.6 w/w% agarose solution in DI water, which has a similar Young's modulus to a mouse brain.[23] The Young's modulus of the probe, determined by the value of the Kapton film substrate, is estimated to be ≈ 4.0 GPa. The photograph demonstrates that the probe can penetrate the agarose model with minimal damage to the biochemical interface and gold traces.

Figure 6D and S15 present the calibration curve for the 50 by 50 μm and 100 by 100 μm glutamate probe, respectively, created by using a modified functionalization protocol (see Experimental Section for details): The procedure starts with adding 0.05 μL of 20 $\mathrm{mg\,mL^{-1}}$ TTF to the anode and 0.05 μL of the Pt-C/Nafion mixture to the cathode. Drop-casting 0.5 μL of GlutOx at a concentration of 100 $\mathrm{U\ mL^{-1}}$ periodically to the surface of the anode minimizes the overflowing of the enzyme solution from the electrode surface. The 50 by 50 μm glutamate probe exhibits good linearity over the testing range ($R^2 > 0.92$) and a sensitivity of 167.13 $\mathrm{mV\,mM^{-1}}$ using a 250 MΩ resistor and 10X amplification. To further demonstrate the flexibility of the device, Figure S16 presents the performance and calibration curve for the 50 by 50 μm glutamate probe before and after 100 bending cycles with a bending radius of 8 mm. The inset plot shows a minimal level of relative decay (3 %) in sensitivity due to bending, which indicates the stability in electrochemical properties of the device after deformation.

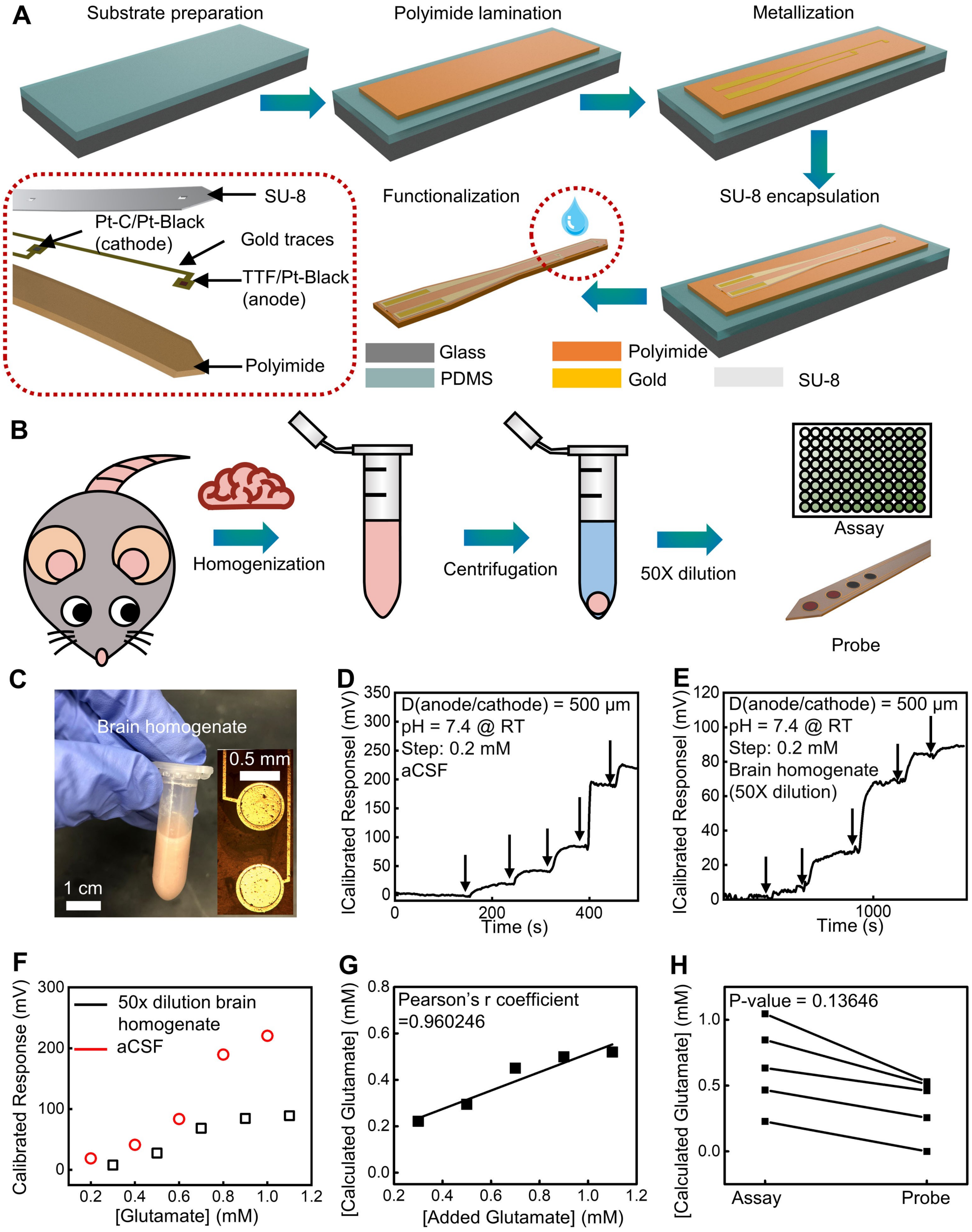

Figure 5. Performance of the glutamate biofuel cell in aCSF and brain tissue homogenate dilutions. (A) Schematic illustration of the fabrication procedure for the biofuel cell-inspired flexible glutamate probe. (B) Schematic illustration of collecting brain homogenate for experimentation with the glutamate assay and microfabricated probe. (C) Photograph and microscopic image of the brain homogenate and glutamate probe used for the study. (D) Change in measured potential of the glutamate probe in aCSF with a stepwise increase in glutamate concentration (0.2 mM). (E) Change in measured potential of the glutamate probe in 50x dilution of brain homogenate with a stepwise increase in glutamate concentration (0.2 mM). (F) Calibration curves of glutamate probe in 50x dilution brain homogenate and aCSF. (G) Pearson's R coefficient for the calculated glutamate concentration vs. the actual glutamate concentration for the 50x dilution brain homogenate. (H) Comparison of calculated glutamate concentrations between the glutamate assay and the glutamate probe.

The study utilizes the hippocampal circuit in mice to evaluate the performance of the miniaturized probes in detecting synaptically released glutamate, as shown in Figure 6E: When Schaffer collateral fibers originating from CA3 neurons are stimulated electrically using a bipolar electrode, glutamatergic synaptic vesicles undergo exocytosis in the CA1 Stratum Radiatum region (Figure 6F). Subsequently, glutamate is released from the presynaptic neuron into the synaptic cleft via exocytosis. Excitatory amino acid transporters (EAAT) will then facilitate the uptake of glutamate and transport glutamate from the synaptic cleft back into the neurons and astrocytes, thereby reducing the overall glutamate concentration in the extracellular space and preventing the continuous firing of action potentials (indicated by blue arrows). Figure 6G and H depict the experimental setup, which includes a stimulation electrode

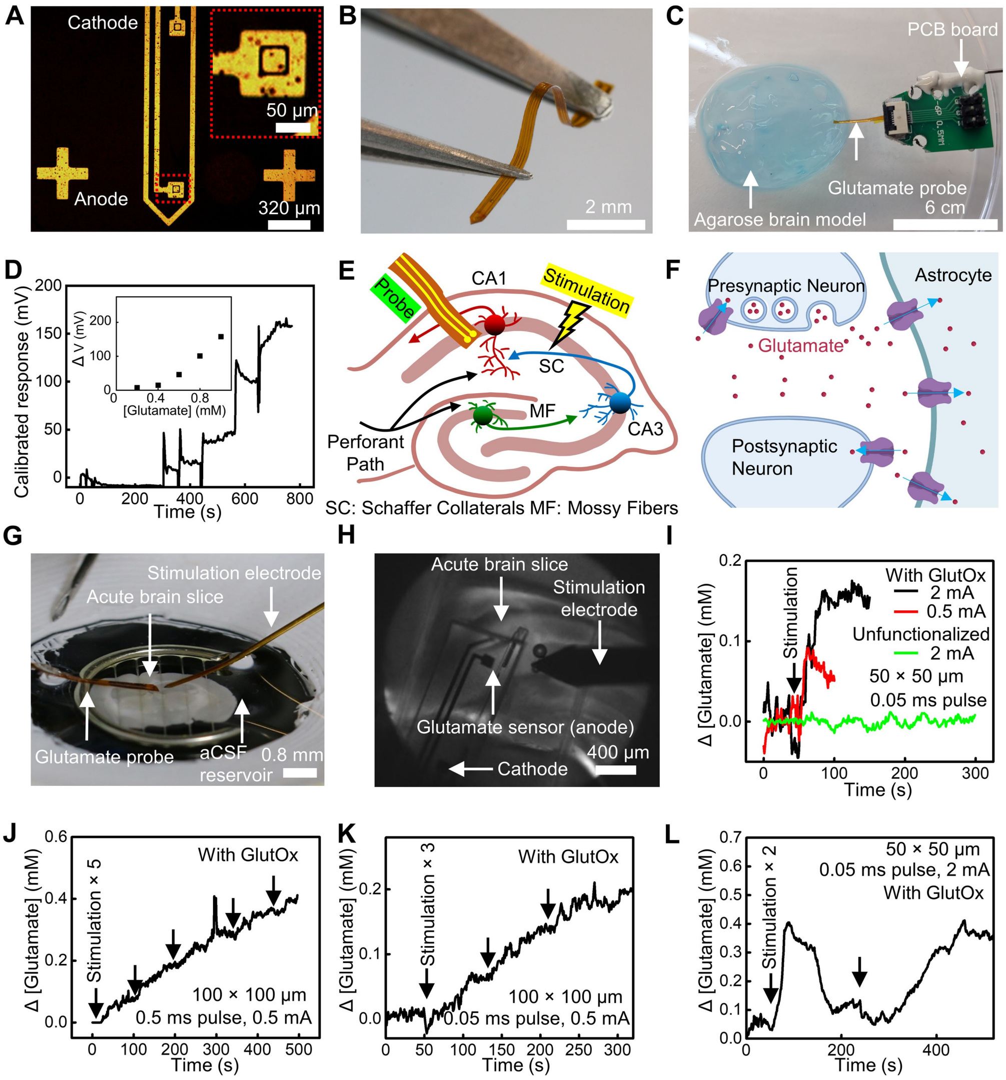

Figure 6. Ex vivo study of dynamic glutamate release from the hippocampal circuit in mice using miniaturized glutamate probes. (A) Microscope image of a 50×50 μm probe. (B) Photograph of a miniaturized probe in a bent configuration. (C) Photograph of a probe penetrating into a 0.6% (w/w) agarose brain model. (D) Change in electric potential measured by the 50×50 μm glutamate probe in aCSF with a stepwise increase in glutamate concentration (0.2 mM). Inset: extracted calibration plot. (E) Schematic illustration of the hippocampal circuit in mice and the stimulation/sensing protocols used in this study. (F) Schematic illustration showing the glutamate release and uptake process. This image is created using Biorender.com. (G) Photograph showing the experimental setup for the ex vivo study using a glutamate probe and a stimulation electrode on a mouse brain slice (thickness: 300 μm). (H) Microscopic image of the glutamate probe and the stimulation electrode on the brain slice. The distance between the stimulation electrode and the probe is approximately 400 μm. The cathode of the glutamate probe is in the surrounding aCSF but not in direct contact with the hippocampus. (I) Change in glutamate concentration detected using a miniaturized probe following electrical stimulation with different pulse intensities (2 mA and 0.5 mA), and comparison with results obtained using an unfunctionalized probe (pulse width: 0.05 ms). (J) Change in glutamate concentration with five repeated pulses (intensity: 0.5 mA, width: 0.5 ms) measured using a miniaturized probe. (K) Change in glutamate concentration with three repeated pulses (intensity: 0.5 mA, width: 0.5 mA) measured using a miniaturized probe. (L) Change in glutamate concentration with two repeated pulses (intensity: 2 mA, width: 0.05 mA) measured using a miniaturized probe showing the increase and decrease process.

and a glutamate probe laminated onto the surface of the CA1 region of the hippocampus. Figure 6I shows changes in local glutamate concentration obtained using the probe with and without key functional layers on the anode (i.e., TTF and GlutOx) (raw data of recorded changes in potential in Figure S17). All stimulations use a bi-phasic pulse width of 0.05 ms. The results suggest an immediate increase in the recorded signal following the stimulation, as detected using the functionalized probe, whereas the signal captured by the unfunctionalized probe remains constant due to the lack of bio-recognition elements for glutamate. The increased voltage indicates the successful detection of the synaptic release event using the glutamate probe following the hippocampal circuit model depicted in Figure 6E and F. For the same functionalized probe, increasing the intensity of the stimulation current (from 0.5 to 2 mA) results in an increased amplitude in detected glutamate concentration, possibly due to more axons being recruited by larger stimulus intensity, resulting in more synaptic release. It is important to note that the observed changes in glutamate concentration (approximately 0.05 mM to 0.15 mM) are lower than the reported values in the extracellular space according to the literature.[11b] One possible explanation for this observation could be that, in this study, the probe is laminated onto the surface of the brain slice rather than penetrating through the tissue. This may have caused any glutamate to diffuse across the surface of the brain tissue and into the surrounding aCSF reservoir, resulting in a lower glutamate concentration and a longer response time.

The data in Figure 6J and S18 illustrate the progressive rise in glutamate concentration, as measured by a 100 by 100 μm probe, during five consecutive stimulations (as indicated by the arrows) with a pulse width of 0.5 ms and a current intensity of 0.5 mA. Each pulse results in the release of a similar amount of glutamate in the local area, creating a stepwise pattern. Figure 6K and S19 depict the outcomes obtained using the same 100 by 100 μm probe from a comparable 0.5 mA pulse stimulation, but with a stimulation period of 0.05 ms. The results indicate that in this experimental setup, increasing the pulse width does not have a significant impact on the amount of glutamate released from each stimulation. With a single pulse (width: 0.05 ms, intensity: 2 mA) applied, and no further stimulations over a period of approximately 300 s, the concentration of glutamate gradually decreases and returns to the baseline (as depicted in Figure 6L and S20). This observation is likely due to a combined effect of glutamate uptake by transporters in the extracellular space, as well as diffusion in the solution.[24] The glutamate probe exploited in this study has a sensing area of 50 by 50 μm, and as a result, it will detect changes in glutamate concentration from extracellular space as well as peri-synaptic sites within this area. The sensing result presented in this study suggests the glutamate spillover from the synaptic cleft despite the role of astrocytes in helping to maintain glutamate homeostasis. The observation may occur due to the following reason: The brain is packed with synapses at a density of ≈2 synapses per μm^3.[25] Synaptically released glutamate can escape from the synaptic clefts, diffuse into the extracellular space, and activate extrasynaptic glutamate receptors.[25a,26] The result is also consistent with a recent report that single synapse-released glutamate can spread into the extracellular space as far as 1.5 μm.[27] Following the application of another pulse, the signal increases once more and reaches a similar amplitude as expected. Notably, the observed signal increase does not necessarily imply a continuous or sustained release of glutamate throughout the entire process. A recent study that utilized iGluSnFr has demonstrated that the sustained release of glutamate upon stimulation lasted for approximately 1 s.[28] The response time until reaching saturation, as observed in our study, should be associated with the time it takes for glutamate to diffuse and reach the sensor. To further enhance the monitoring of glutamate release, it may be beneficial to explore the use of needle-type devices in future works. These devices can potentially establish a better interface with target biotissues, allowing for more precise and sensitive measurements of glutamate release/dynamics. Overall, the results obtained indicate the tremendous potential of the miniaturized probes in the quantitative analysis of glutamate release with spatial precision. This could lead to a better understanding of previously unknown molecular and cellular mechanisms underlying the structural and functional reorganization of neural circuits.

It should be noted that the sensing area described in this study is larger than the typical sizes of cells in the central nervous system, and also larger than the size of typical synapses. Consequently, our probe does not have the resolution to detect responses released from a single cell or a single synapse. This makes it challenging to differentiate between the released glutamate from astrocytes and neurons. However, the systematic study presented in this work uncovers essential requirements and considerations for the development of miniaturized sensing probes. As a result, this study serves as a foundation for future applications of the device concept in neuroscience, contingent upon the availability of an improved fabrication resolution. To provide additional evidence of feasibility, we have included supplementary results of the ex vivo test using the cross-section of an isonel-insulated Pt wire with a diameter of 25 μm as the sensing electrode (Figure S21). The resulting device shows a similar response pattern for glutamate release triggered by electrical stimulation, further highlighting the potential of this approach. Additionally, although the amplifier can help minimize the impact of environmental factors, it is not necessarily required for the operation of the device. Figure S22 presents additional ex vivo results obtained using a probe without the amplifier. The observed consistent pattern of signal increase following stimulation provides evidence for the potential development of functional devices that do not require signal amplification. However, it is important to acknowledge that while the design of the sensing platform draws inspiration from the structure of biofuel cells, the current system still relies on the use of a potentiostat for signal readout. As a result, it is not yet capable of functioning as a self-powered sensor system. As shown in Figure S23, the maximum power outputs are 0.14516 $\mu W cm^{-2}$ to 0.22853 $\mu W cm^{-2}$ in 0 to 1.2 mM glutamate solutions, respectively. One possible reason for the low power output values could be the high surface impedance of the electrode. Currently, the measured power output values are below the required power density for driving a bio-integrated display ($\approx 3\, mW cm^{-2}$)[29] or other signal output devices. While further improvements in power output are possible through surface engineering of the electrodes to optimize energy harvesting performance,[8a] the results presented in this study indicate that the current design is adequate for its intended sensing purpose.

We used transgenic mice with GFP expression under the control of the Thy1 promoter to assess the extent of brain damage caused by the insertion of the probe in vivo. In these mice, a subset of neurons including layer V motorneurons in the cortex express GFP, thereby allowing an unbiased evaluation of neuronal damage around the probe insertion site. After performing a craniotomy and carefully removing the dura, the miniaturized probe was slowly lowered (speed: 100 microns/minute) into the sensorimotor cortex at a depth of 600 μm (e.g., layer V). The probe was kept in position for 2 minutes before slow removal. Mice were then perfused (c.a. 10 minutes after the probe was removed) and the brains were dissected and processed for immunohistochemistry. Neuronal cell bodies, dendritic structures and spine morphology remained unaltered around the injection site (Figure 7). Moreover, we did not observe any rapid induction of neuronal cell death based on Caspase-3 immunostaining. It is important to note that Caspase-3 activation during apoptosis is a very rapid process, taking 5 minutes or less to reach completion.[30] Together, these results indicate that the miniaturized structure of the probe leads to minimal brain damage, thereby enabling glutamate sensing without potential confounding variables.

Conclusion

In summary, this study illustrates the feasibility of utilizing a biofuel cell design in a flexible and miniaturized sensing probe to enable the continuous, real-time detection of glutamate in complex biological environments. The findings indicate that the biofuel cell configuration exhibits sensitivity to glutamate, with detectable concentrations spanning from about 0.05 mM to 1.0 mM. This research comprises comprehensive investigations of critical parameters that influence the sensing performance, as well as the necessary requirements and considerations for constructing miniaturized sensing probes. Testing the resulting sensing platform with biological samples, including 50X dilutions of mouse brain homogenates and mouse brain slices, validates the effectiveness of the system. The results obtained from experiments utilizing the hippocampal circuit in mice suggest that the miniaturized probes can detect synaptically released glutamate triggered by electrical stimulation. Future studies will aim to explore changes in glutamate concentrations in different regions of the brain, such as the cortex or the ventral tegmental area (VTA), by employing miniaturized probes.

Additional efforts will focus on further reducing the overall size of the electrode for improved spatial resolution, enhancing the sensitivity, and minimizing the overall variation in sensitivity between devices. Furthermore, incorporating other wireless components, such as a Bluetooth or NFC chip, could improve the device's implantability and enable potential in vivo testing. This device could have potential applications in glutamate concentration mapping

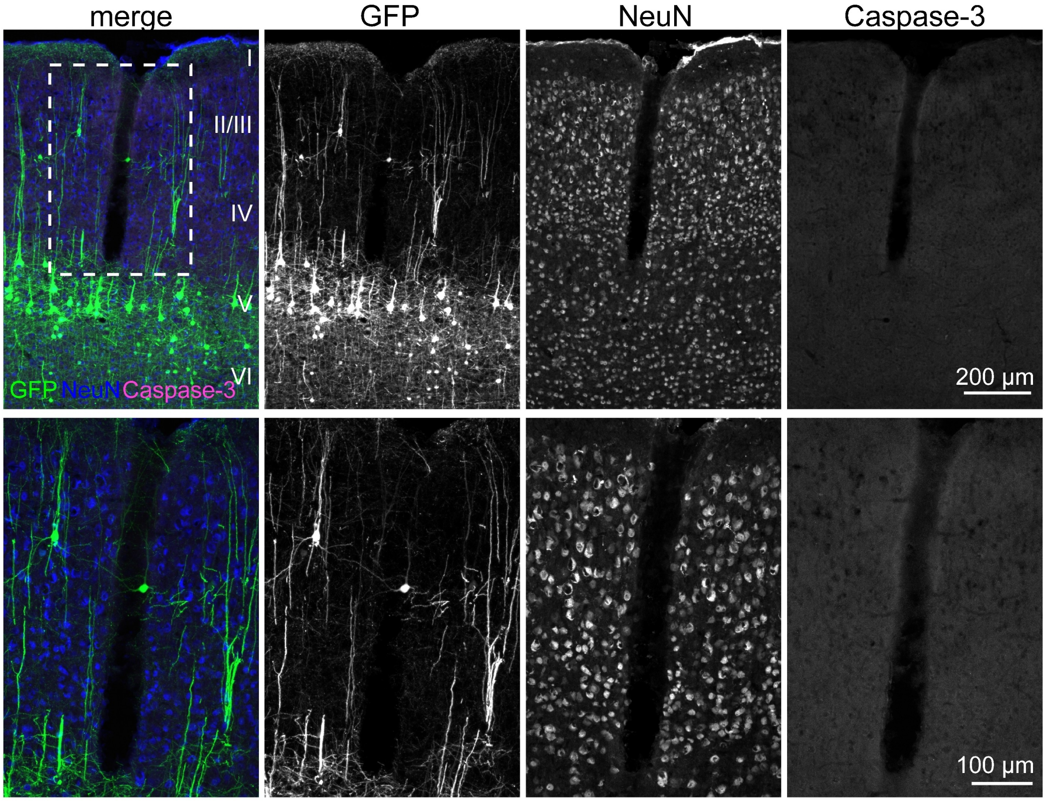

Figure 7. Results of immunohistochemistry showing that in vivo implantation of the glutamate sensor does not induce neuronal damage. The glutamate sensor was slowly inserted into the cortex of Thy1-GFP mouse at a depth of 600 μm. Top row: Sagittal section of the mouse cortex showing the dendritic and cellular structure of GFP-expressing neurons. The brain tissue was also immunostained with NeuN and Caspase-3 antibodies. Roman numerals indicate cortical layers. The insertion location of the glutamate sensor is clearly visible. Bottom row: the magnified images of the area containing the sensor insertion site that was highlighted with the dashed line in the top row.

with high spatial and temporal resolution. A multiplexed system that incorporates an array of miniaturized anodes connected to a common cathode could enable the mapping of glutamate concentration across various brain regions simultaneously. Disease state models of TBI could be utilized to investigate the extent to which glutamate concentration increases in distinct brain regions and their correlation with elevated neuronal firing activity. Therefore, a multiplexed device could have diagnostic potential for detecting the onset and progression of brain injury by enabling the real-time monitoring of glutamate concentrations across multiple brain regions. Additionally, to enhance the diagnostic accuracy of the device, it would be valuable to increase the detection speed of the sensor, enabling it to recognize rising levels of glutamate concentration within a few milliseconds. This improvement would allow the device to detect increases in glutamate concentration resulting from each individual action potential, making it a useful tool for mapping out glutamate cell signaling pathways in both healthy and diseased states. This technology could be particularly beneficial to healthcare professionals by aiding in the early detection of diseases like stroke, epilepsy, and schizophrenia that can be caused by elevated levels of glutamate.

Supporting Information

The authors have cited additional references within the Supporting Information.[31]

Acknowledgements

This work was supported by The Ohio State University start-up funds (to J.L.), the National Science Foundation (award number: ECCS-2223387, to J. L.) the Chronic Brain Injury Pilot Award Program at The Ohio State University (to J.L., W.S. and A.T.), The Ohio State University Center for Medical and Engineering Innovation pilot grant (to J.L.), National Center for Advancing Translational Sciences (award number: UL1TR002733), and National Institute of Neurological Disorders and Stroke (award number: R01NS124714, to W.S.). The content was solely the responsibility of the authors and did not necessarily represent the official views of the National Center for Advancing Translational Sciences or the National Institutes of Health. This work was also supported by the Ohio State University Materials Research Seed Grant Program, funded by the Center for Emergent Materials; NSF-MRSEC, grant DMR-2011876; the Center for Exploration of Novel Complex Materials; and the Institute for Materials Research.

Conflict of Interest

P.N., T.-L.L., S.C., and J.L. are inventors on a pending patent filed by the Ohio State University (application no.: 63/359,660, filing date: July 08, 2022.). The other authors declare no competing financial interests.

Data Availability Statement

The data that support the findings of this study are available from the corresponding author upon reasonable request.

Keywords: Biofuel Cells · Bioimplants · Flexible Electronics · Glutamate · Neurochemical Sensors

[1] a) Martin, J. Kim, J. F. Kurniawan, J. R. Sempionatto, J. R. Moreto, G. Tang, A. S. Campbell, A. Shin, M. Y. Lee, Liu, X. Liu, J. Wang, *ACS Sens.* **2017**, *2*, 1860–1868; b) J. Kim, A. S. Campbell, J. Wang, *Talanta* **2018**, *177*, 163–170; c) W. Gao, S. Emaminejad, H. Y. Y. Nyein, S. Challa, K. Chen, A. Peck, H. M. Fahad, H. Ota, H. Shiraki, D. Kiriya, D.-H. Lien, G. A. Brooks, R. W. Davis, A. Javey, *Nature* **2016**, *529*, 509–514; d) T. Arakawa, Y. Kuroke, H. Nitta, P. Chouhan, K. Toma, S.-I. Sawada, S. Takeuchi, T. Sekita, K. Akiyoshi, S. Minakuchi, K. Mitsubiyashi, *Biosens. Bioelectron.* **2016**, *84*, 106–111; e) H. Lee, Y. J. Hong, S. Baik, T. Hyeon, D.-H. Kim, *Adv. Healthcare Mater.* **2018**, *7*, 1701150; f) J. Andreu-Perez, D. R. Leff, H. M. D. Ip, G.-Z. Yang, *IEEE Trans. Biomed. Eng.* **2015**, *62*, 2750–2762; g) R. Li, H. Qi, Y. Ma, S. Liu, Y. Jie, J. Jing, J. He, X. Zhang, L. Wheatley, C. Huang, X. Sheng, M. Zhang, L. Yin, *Nat. Commun.* **2020**, *11*, 3207; h) G. Rong, E. H. Kim, Y. Qiang, W. Di, Y. Zhong, X. Zhao, H. Fang, H. A. Clark, *ACS Sens.* **2018**, *3*, 2499–2505.

[2] a) W. J. McEntee, T. H. Crook, *Psychopharmacology* **1993**, *111*, 391–401; b) Y.-T. Li, X. Jin, L. Tang, W.-L. Lv, M.-M. Xiao, Z.-Y. Zhang, C. Gao, G.-J. Zhang, *Anal. Chem.* **2019**, *91*, 8229–8236.

[3] P.-M. Herminia, K. Tuz, *Contrib. Nephrol.* **2006**, *152*, 221–240.

[4] a) C. Baliatsas, J. Bolte, J. Yzermans, G. Kerlfkens, M. Hooiveld, E. Lebert, I. V. Kamp, *Int. J. Hyg. Environ. Health* **2015**, *218*, 331–344; b) M. Cruz-Haces, J. Tang, G. Acosta, J. Fernandez, R. Shi, *Transl. Neurodegener.* **2017**, *6*, 20; c) J. Schultz, Z. Uddin, G. Singh, M. M. R. Howlader, *Analyst* **2020**, *145*, 321–347.

[5] J. Castillo, M. I. Loza, D. Mirelman, J. Brea, M. Blanco, T. Sobrino, F. Campos, *J. Cereb. Blood Flow Metab.* **2016**, *36*, 292–301.

[6] J. S. Marvin, B. Scholl, D. E. Wilson, K. Podgorski, A. Kazemipour, J. A. Muller, S. Schoch, F. J. U. Quiroz, N. Rebola, H. Bao, J. P. Little, A. N. Tkachuk, E. Cai, A. W. Hantman, S. S.-H. Wang, V. J. Dipiero, B. G. Borghuis, E. R. Chapman, D. Dietrich, D. A. Digregorio, D. Fitzpatrick, L. L. Looger, *Nat. Methods* **2018**, *15*, 936–939.

[7] a) Y. Sun, T. N. H. Nguyen, A. Anderson, X. Cheng, T. E. Cage, J. Lim, Z. Zhang, H. Zhou, F. Rodalakis, Z. Zhang, I. Arslan, S. Ramanathan, H. Lee, A. A. Chubykin, *ACS Appl. Mater. Interfaces* **2020**, *12*, 24564–24574; b) X.-K. Yang, F.-L. Zhang, Y. Tang, J. Yan, Y.-L. Liu, C. Armatore, W.-H. Huang, *Angew. Chem. Int. Ed.* **2021**, *60*, 15803–15808; c) W. Wei, Y. Song, L. Wang, S. Zhang, J. Luo, S. Xu, X. Cai, *Microsyst. Nanoeng.* **2015**, *1*, 15002; d) Y. Wang, H. Fathali, D. Mishra, T. Olsson, J. D. Keighron, K. P. Skibicka, A.-S. Cans, *J. Am. Chem. Soc.* **2019**, *141*, 17507–17511; e) J. Xie, Y. Dai, Y. Xing, Y. Wang, G. Yang, E. He, Z. Xu, P. Fan, F. Mo, Y. Wu, Y. Song, X. Cai, *ACS Sens.* **2023**, *8*, 1810–1818.

[8] a) Y. Yu, J. Nassar, C. Xu, J. Min, Y. Yang, A. Dai, R. Doshi, A. Huang, Y. Song, R. Gehlhar, A. D. Ames, W. Gao, *Sci.*

Rob. **2020**, *5*, eaaz7946; b) X. Chen, L. Yin, J. Lv, A. J. Gross, M. Le, N. G. Gutierrez, Y. Li, I. Jeerappan, F. Giroud, A. Berezovska, R. K. O'Reilly, S. Xu, S. Cosnier, J. Wang, *Adv. Funct. Mater.* **2019**, *29*, 1905785.

[9] a) J. Bandodkar, P. Gutruf, J. Choi, K. Lee, Y. Sekine, J. T. Reeder, W. J. Jeang, A. J. Aranyosi, S. P. Lee, J. B. Model, R. Ghaffari, C.-J. Su, J. P. Leshock, T. Ray, A. Verrillo, K. Thomas, V. Krishnamurthi, S. Han, J. Kim, S. Krishnan, T. Hang, J. A. Rogers, *Sci. Adv.* **2019**, *5*, eaav3294; b) X. Jin, A. J. Bandodkar, M. Fratus, R. Asadpour, J. A. Rogers, M. A. Alam, *Biosens. Bioelectron.* **2020**, *168*, 112493.

[10] N. F. Almeida, A. K. Mulchandani, *Anal. Chim. Acta* **1993**, *282*, 353–361.

[11] a) K. Hashimoto, G. Engberg, E. Shimizu, C. Nordin, L. H. Lindström, M. Iyo, *BMC Psychiatry* **2005**, *5*, 6; b) K. Moussawi, A. Riegel, S. Nair, P. W. Kalivas, *Front. Syst. Neurosci.* **2011**, *5*, 94.

[12] P. Rewatkar, J. U. S., S. Goel, *ACS Sustainable Chem. Eng.* **2020**, *8*, 12313–12320.

[13] M. E. Payne, A. Zamarayeva, V. I. Pister, N. A. D. Yam()-amoto, A. C. Arias, *Sci. Rep.* **2019**, *9*, 13720.

[14] Y. Jee, Y. K. Cho, S. Granick, T. Tlusty, *Proc. Natl. Acad. Sci. USA* **2018**, *115*, E10812–E10821.

[15] D. H. A. Hameed, E. H. Ali, *Arch. Inst. Razi* **2021**, *76*, 769–779.

[16] T. Adachi, Y. Kitazumi, O. Shirai, K. Kano, *Sensors* **2020**, *20*, 4826.

[17] X. E. Wu, Y. Z. Guo, M. Y. Chen, X. D. Chen, *Electrochim. Acta* **2013**, *98*, 20–24.

[18] M. M. Rahman, T. Yamazaki, T. Ikeda, M. Ishida, K. Sawada, *TRANSDUCERS 2009–2009 International Solid-State Sensors, Actuators and Microsystems Conference*, Denver, CO, USA, **2009**, pp. 88–91.

[19] a) M. A. Bunin, R. M. Wightman, *J. Neurosci.* **1998**, *18*, 4854–4860; b) G. W. Arbuthnott, J. Wickens, *Trends Neurosci.* **2007**, *302*, 62–69.

[20] a) Z. Li, Y. Song, G. Xiao, F. Gao, S. Xu, M. Wang, Y. Zhang, F. Guo, J. Liu, Y. Xia, X. Cai, *Anal. Biochem.* **2018**, *550*, 123–131; b) K. Hashimoto, T. Ishima, Y. Sato, D. Bruno, J. Nierenberg, C. R. Marmar, H. Zetterberg, K. Blennow, N. Pomara, *Sci. Rep.* **2017**, *7*, 3485.

[21] M. Lazouskaya, O. Scheler, V. Mikli, K. Uppuluri, K. Zaraska, M. Tamm, *J. Electrochem. Soc.* **2021**, *168*, 107511.

[22] W. Al-Graiti, J. Foroughi, Y. Liu, J. Chen, *ACS Omega* **2019**, *4*, 22169–22177.

[23] Y. Park, C. K. Franz, H. Ryu, H. Luan, K. Y. Cotton, J. U. Kim, T. S. Chung, S. Zhao, A. Vazquez-Guardado, D. S. Yang, *Sci. Adv.* **2021**, *7*, eabf9153.

[24] S. A. Hires, Y. Zhu, R. Y. Tsien, *Proc. Natl. Acad. Sci. USA* **2008**, *105*, 4411–4416.

[25] a) D. A. Rusakov, D. M. Kullmann, *J. Neurosci.* **1998**, *18*, 3158–3170; b) N. Uppal, R. Puri, F. Yuk, W. G. Janssen, O. Bozdagi-Gunal, H. Harony-Nicolas, D. L. Dickstein, J. D. Buxbaum, P. R. Hof, *Mol. Autism* **2015**, *6*, 41.

[26] a) D. A. Rusakov, *Biophys. J.* **2001**, *81*, 1947–1959; b) K. Zheng, A. Scimemi, D. A. Rusakov, *Biophys. J.* **2008**, *95*, 4584–4596.

[27] E. A. Matthews, W. Sun, S. M. McMahon, M. Doengi, L. Halka, S. Anders, J. A. Müller, P. Steinlein, N. S. Vana, G. van Dyk, J. Pitsch, A. J. Becker, A. Pfeifer, E. T. Kavalali, A. Lamprecht, C. Henneberger, V. Stein, S. Schoch, D. Dietrich, *Cereb. Cortex* **2022**, *32*, 3669–3689.

[28] M. P. Parsons, M. P. Vanni, C. L. Woodard, R. Kang, T. H. Murphy, L. A. Raymond, *Nat. Commun.* **2016**, *7*, 11251.

[29] T. Stuart, J. Hanna, P. Gutruf, *APL Bioeng.* **2022**, *6*, 021502.

[30] L. Tyas, V. A. Brophy, A. Pope, A. J. Rivett, J. M. Tavaré, *EMBO Rep.* **2000**, *1*, 266–270.

[31] Y. Umasankar, B.-R. Adhikari, A. Chen, *Bioelectrochemistry* **2017**, *118*, 83–90.

Manuscript received: July 18, 2023
Accepted manuscript online: August 26, 2023
Version of record online: September 13, 2023